Highly Efficient, Zero-Skew, Integrated Clock Distribution Networks Using Salphasic Principles

Andrei PAŞCA[1,2], Mircea CIUGUDEAN[2]
[1]*Continental Automotive Romania, Timişoara, 300704, Romania*
[2]*Politehnica University of Timişoara, 300006, Romania*
andrei.pasca@continental-corporation.com

***Abstract*—The design of highly efficient clock distributions for integrated circuits is an active topic of research as there will never be a single solution for all systems. For high performance digital or mixed-signal circuits, achieving zero-skew clock over large areas usually comes with high costs in power requirements and design complexity. The present paper shows an overview of a recently proposed technique for ICs - on-die salphasic clock distribution, introduced by the author for CMOS processes. Initially reported in literature for rack-systems, the present paper shows that further refinements are needed for the concept to be applicable on a silicon die. Based on the formation of a standing wave (intrinsically presenting extended in-phase regions) with a voltage peak at the input (creating a no-load condition), it is shown that any IC implementation must use transmission lines loss compensation techniques to maintain the proper standing wave configuration. Furthermore, the paper shows theoretical solutions and describes practical on-die techniques for pseudo-spherical bidimensional surfaces, which, with the already reported orthogonal and pseudo-orthogonal structures, can be used to distribute with minimal power requirements a zero-skew clock signal, over large silicon areas.**

***Index Terms*—bi-dimensional clock distribution, loss compensation, salphasic, standing wave, zero-skew.**

I. INTRODUCTION

An essential part of every high performance synchronous integrated circuit (IC) is its clock distribution network – without it, system operation and performance cannot be guaranteed at the specified frequency. As detailed in [1], proper system operation requires the existence of a specific alignment between the active edges of the clock signal and the data processing paths. Given the very nature of the clock signal – i.e. having the maximum frequency in a system, while, in the same time, having the highest capacitive load – designing a good clock distribution network takes not only a large part of the project's total time schedule, but also an important fraction of the power budget [2-4], reaching up to about half of total system power.

Various techniques were proposed for dealing with the most critical aspects of good clock distribution networks – the power consumption and the clock skew. For instance, when talking about clock skew, a designer can choose between different tree topologies (buffered trees [5-7], symmetric H or X trees [1]), different post fabrication re-alignment techniques – using phase locked loops, delay line loops or distributed synchronized oscillators [8-11] or using programmable delay elements [8], [12-16]. The complexity of the system is rising from the first to the last approaches. However, so does the system's performance as the post-fabrication de-skewing allows for tighter design timings.

For the power dissipation problem, inspecting the known formula for the dynamic power used to charge and discharge the capacitance C_{CK} with a voltage V_{SWING} at the operating f_{CK} frequency, $P_d = f_{CK} \cdot C_{CK} \cdot V_{SWING}^2$, it becomes evident there are only a few possible strategies with an impact on system performance. A designer may try to reduce the operating frequency, but this comes with an increase in the parallelism and hence, in a larger clock capacitance. The only relatively free parameter and with the biggest overall impact due to the quadratic dependence, is the voltage swing. For this reason, [3-4], [17-21] are all trying to decrease system power by reducing the clock signal's amplitude. As a cautionary note, the total power gain may not be as significant as the previous formula may indicate. If the swing reduction is achieved by using linear techniques, the quadratic dependence will be lost, so a 50% amplitude reduction will yield only 50% power reduction.

All these techniques rely on classic principles for which the propagation delays are unwanted side effects that must be eliminated. As the operating clock frequencies are placed already in the microwave range and the chip sizes (5 – 10mm on a side) are comparable with the signal wavelengths (10mm to several centimeters), another class of clock distribution techniques becomes possible – i.e. resonant or standing wave based distributions. Here, the clock source is no longer a point source but, instead, is spread over the entire IC surface. For instance, in [22-23], the loading of the clock network is used as a distributed capacitance for an LC oscillator tank, with the inductor either external [22] or internal [23].

References [24-25] are taking profit also of the transmission line properties of the clock networks. Here, line segments are used both as equivalent resonant elements and as supports for signal distribution. This combination of non-localized signal generation and propagation allows the formation of standing waves, with the advantage that extended, same-phase – i.e. zero skew – regions are created over the silicon area as an intrinsic property of the standing wave.

The net benefit for the techniques used in [21-25] is the important reduction in the power needed to drive the clock network. For the resonant networks of [22-23], the injected energy is cycled between the reactive components – once the clock distribution reaches the steady state, the system

Digital Object Identifier 10.4316/AECE.2016.01010

will use power only for sustaining the oscillations. This power is only a fraction of that needed to fully charge and discharged the same capacitive load. This is also valid for the distributions of [21], [24-25] with the difference that the initial energy is transported as direct and reflected waves.

Although not at integrated circuit level, [26-27] demonstrated another standing wave distribution principle. Similarly with [21], [25], the salphasic approach, as named in the references, uses the standing wave configuration to address the skew problem. The power dissipation problem is further avoided by the careful selection of the termination impedance used for the creation of total reflection condition. By properly choosing the value of the load impedance it is possible to place a voltage peak at the input node. Form the clock generator's point of view, this voltage anti-node translates in a no-load condition. Unlike the resonant techniques for which the distributed frequency is set mainly by physical system dimensions, the salphasic distribution can be tuned with the aid of the termination impedance, allowing for a wider operating range.

As a note, this paper will use the word salphasic as a qualifier that denotes a standing wave having a particular pattern – i.e. the existence of a total reflection condition at the load with a voltage peak at the generator's point (that is a no load condition) and the extended same-phase regions.

The technique of [26-27] is applied at a rack-system level, but, as was first introduced by the author of the present paper in [28], the approach may be extended also for integrated clock distributions built directly on the silicon substrate. Furthermore, as it was suggested initially in [26], the technique can be generalized for extended surfaces, with net benefits with respect to power dissipation and clock skew.

As it will be seen, any integrated salphasic clock distribution needs a transmission line loss compensation technique. As a note, this is also valid for the resonant or standing wave structures that are using transmission line segments of [24-25]. However, do to the oscillatory nature of those clock distributions, the loss compensation is achieved in the unitary oscillator cells. Compensating the integrated transmission line losses is not a new topic, as extensive research is done on this for distributed amplifiers and RF applications [29-31]. The topic is also researched for digital ICs where various techniques were proposed to improve the clock distribution network [32] or to compensate the propagation delays of the signal paths [33-35].

The circuit configurations proposed in [32] or [35] have two major drawbacks for the salphasic distribution. The first drawback comes from the limitation of the voltage swing imposed by the source degeneration circuit. The second drawback comes from the limited online trimming possibilities as the circuits would need to adjust physical source degeneration resistors. So once built, these compensation cells will be highly dependent on the resulting process corner. As it was shown in [36], based on a classic cell (cross-connected inverter pair) it is possible to obtain an adjustable negative impedance circuit, well suited for standing wave based distributions.

For the frequency range, the oscillating distribution networks require a strong correlation between the lengths of the trace segments and the oscillation frequency and can be operated only around the self-resonant frequency (or its harmonics). For the salphasic distributions, the formation of the salphasic standing wave pattern depends on the structure's termination impedance that provides the total reflection condition. By properly choosing the termination network (which can be external to the IC), the user may tune the distribution to any operating frequency.

Although the salphasic technique is not new per se, the novelty comes from its application at an IC level, by using loss compensation techniques and from the extension of the distribution over bi-dimensional silicon areas. With these, the technique proves to be a highly efficient method of distributing a zero-skew, high frequency clock signal with minimal power consumption.

II. On-die Integrated Salphasic Clock Distribution

Assuming a (complex) harmonic signal applied at the input of the transmission line, similarly with [26] and [28], the standing wave can be determined based on the complex solutions of the transmission line equations.

$$u(x,t)=U_0^D \cdot e^{j\cdot\omega t} \cdot e^{-\gamma\cdot x} + U_0^R \cdot e^{j\cdot\omega t} \cdot e^{\gamma\cdot x} \tag{1}$$

$$\gamma = \alpha + j \cdot \beta \tag{2}$$

In the line-voltage solution (1), $U_0{}^D$ and $U_0{}^R$ stand for the direct and reflected waves amplitudes as seen at the generator's node, while the complex propagation constant γ of (2), determines the attenuation constant α and the phase constant β. The time dependent complex exponentials represent the harmonic signal.

For the lossless case, where the propagation constant γ is imaginary, and assuming total reflection at the far end of the transmission line, the amplitudes of the direct and reflected waves will be equal to U_0 at all points. With an arbitrary phase shift φ in the reflected wave, the solution of the line voltage can be written as in (3) [26], [28]:

$$u(x,t) = U_0 \cdot e^{j\cdot\omega\cdot t} \cdot \left(e^{-j\cdot\beta\cdot x} + e^{j\cdot\varphi} \cdot e^{j\cdot\beta\cdot x}\right) \tag{3}$$

From (3), the solution for the standing wave becomes:

$$u(x,t) = 2 \cdot U_0 \cdot e^{j\left(\omega\cdot t+\frac{\varphi}{2}\right)} \cdot \cos\left(\beta\cdot x+\frac{\varphi}{2}\right) \tag{4}$$

In (4) it can be seen that the position dependent part (the cosine function) is completely independent of the time varying part (the complex exponential). This property explains the existence of the extended same-phase regions with steep 180 degrees phase steps at the zero crossings of the cosine, as illustrated in fig. 1. As the salphasic distribution requires the presence of a voltage anti-node at the origin of the system, based on (4), the phase shift φ, introduced by the line termination must be strictly zero.

One of the key parameters for the salphasic operation is the propagation loss of the structure. As it was shown in [26] for the system level, once the transmission lines used are non-ideal, the standing wave no longer presents the extended same-phase regions. While [26] discussed the effects of the transmission lines losses, it did not offer any bounds for the attenuation coefficient for which the salphasic behavior is still acceptable. For the IC's case, the problem is even more stringent if no special measures are taken, but, as it will be seen here for the first time, a design constraint for the acceptable attenuation constant may be

derived.

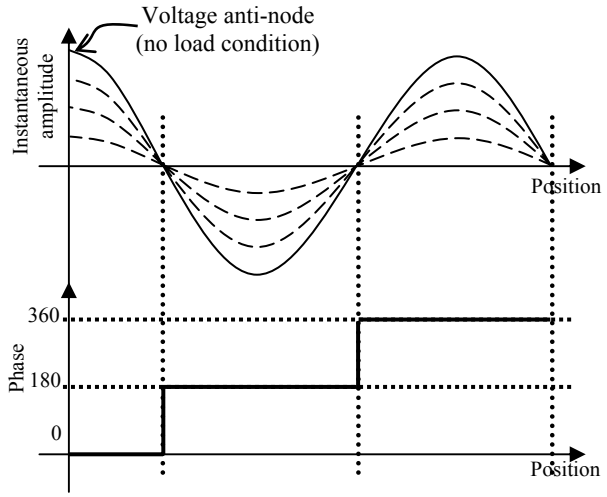

Figure 1. Standing wave for the amplitude and the phase of the line voltage

Similar with [26] and [28], assuming a lossy transmission line (with small enough losses to allow reasonable approximations), the voltage standing wave may be described starting from the general form of the solution as in (5) and (6):

$$u(x,t)=U_0^D\cdot e^{j\cdot\omega t}\cdot e^{-\alpha\cdot x}\cdot e^{-j\cdot\beta\cdot x}+U_0^R\cdot e^{j\cdot\omega t}\cdot e^{\alpha\cdot x}\cdot e^{j\cdot\beta\cdot x} \quad (5)$$

$$U_0^R=U_0^D\cdot e^{-2\cdot\alpha\cdot d} \quad (6)$$

As the amplitude of direct wave $U_0{}^D$ at the generator's node is identical for both the lossless and the lossy case, for a direct comparison with the former case, it is assumed to be equal with U_0 as in (3). In (6), the amplitude of the reflected wave $U_0{}^R$, as seen at the generator node, is given by the amplitude of the direct wave affected by the attenuation constant α both for the flight and the return trip. The load is assumed being at d coordinate away from the generator.

By manipulating (5) to bring it to a form similar with (4), it is possible to estimate the effect of the attenuation constant on the standing wave:

$$\begin{aligned}u(x,t)=&\,2\cdot U_0\cdot e^{-\alpha\cdot x}\cdot e^{j\cdot\omega t}\cdot\cos(\beta\cdot x)-\\&-2\cdot U_0\cdot e^{-\alpha\cdot x}\cdot e^{j\cdot\omega t}\cdot\alpha\cdot(d-x)\cdot e^{j\cdot\beta\cdot x}\end{aligned} \quad (7)$$

A major difference between (7) and (4) is the presence of a second term depending both on the position coordinate x and on the time instant t. The first term in (7) differs from (4) only through the attenuation constant's effect. As this position dependent function is still a real valued function, the phase behavior of the first term in (7) is similar with that of (4). However, since the new term has a complex dependence on the position coordinate, it will destroy the zero-skew condition.

Starting from the real and imaginary parts of the position dependent terms of (7) it is possible to evaluate the tangent of the phase angle for the standing wave voltage (8).

$$\tan(\Delta\varphi)=-\frac{\alpha\cdot(d-x)}{1-\alpha\cdot(d-x)}\cdot\frac{\sin(\beta\cdot x)}{\cos(\beta\cdot x)} \quad (8)$$

If the effect of the attenuation constant is small enough and using the inverse tangent function, (8) may be further reduced to (9):

$$\Delta\varphi\approx-\arctan(\alpha\cdot(d-x)\cdot\tan(\beta\cdot x)) \quad (9)$$

By assuming small angles, the argument of the complex standing wave voltage for points at a reasonable distance away from voltage nodes (where the tangent is infinite) is given by (10):

$$\Delta\varphi\approx-\alpha\cdot(d-x)\cdot\tan(\beta\cdot x)-\pi\cdot\mathrm{int}\left(\frac{2}{\lambda}\cdot\left(x+\frac{\lambda}{4}\right)\right) \quad (10)$$

Note in (10) the presence of the 180 degrees phase shifts given by the integer function. In addition to these phase steps, (10) contains also an error term that shows the effect of the line losses. Looking at the error term, it can be seen that, as in [26], the magnitude of the phase error decreases towards the load of the transmission line as position x approaches d. Using a setup similar with that simulated in [26] – i.e. 12.7m long RG58 cable at 100MHz (equivalent to a line length d of 6.5 times the wavelength and an attenuation constant α of 0.0185m^{-1}) – and estimating the phase error at 1/8 of the wavelength away from the generator, gives a phase error around 13 degrees (i.e. about 3.7% of the signal's period), compatible with the simulation results presented in [26].

For long lines that allow the existence of several voltage nodes, the phase error exhibits a pseudo-periodic behavior with a period of half the wavelength. For the short salphasic lines that are expected to be found in ICs, where the total length should not allow voltage nodes, the plot of the error term shows only one peak placed between the middle of the line (for very short lines) and the far end of the line. If the line length d is assumed to be, for instance, a quarter of the wave length (yielding a voltage peak at the generator and a voltage node at the load) and estimating the phase error at 90% of the line length it results (11):

$$\Delta\varphi\approx\alpha\cdot 0.1\cdot\frac{\lambda}{4}\cdot\tan\left(0.9\cdot\frac{\pi}{2}\right) \quad (11)$$

Imposing no more than 2% of the clock's period (i.e 10ps for a 2GHz clock) as acceptable skew between theses points, the phase difference may not be larger than $4\cdot\pi/100$. Based on this and using (11), it is possible to estimate the tolerated attenuation constant as in (12):

$$\alpha\le\frac{16\cdot\pi}{10\cdot\lambda\cdot\tan\left(0.9\cdot\frac{\pi}{2}\right)} \quad (12)$$

For a heavily capacitively loaded transmission line, working in the range of 2 to 5GHz, the wavelength λ may be around 20 to 30mm. With these, the tolerated attenuation constant is found to be around 25m^{-1} to 40m^{-1}. Although these values may seem rather large, since an $e^{-2\cdot\alpha\cdot(d-x)}$ exponential term was approximated in order to derive (7) – with an error of -2% – and the right hand side term in (8) or (9) is still small enough to meet the small angle condition (about 12% error), the results obtained using (12) are valid for the considered line.

If the transmission line is built on a silicon substrate using a standard CMOS process, the main contributor factor for the propagation losses is the resistive behavior of the metal layers. Dielectric losses (usually modeled as a conductance term G in the line equations) are introducing only second order effects so, for the purpose of this paper, they will be neglected. From the dielectric losses, the major effect is given by dielectric leakage currents – i.e. gate leakage – and not by the dielectric loss tangent. With these, the attenuation constant may be approximated with:

$$\alpha=\frac{R}{2}\cdot\sqrt{\frac{C}{L}}=\frac{R}{2\cdot Z_{CI}} \quad (13)$$

In (13), R, C and L are the per unit-length parameters of the transmission line and Z_{CI} is the ideal characteristic impedance (i.e. excluding losses). For a line having a width of 20μm built on one of the last metal layers of a standard 130nm CMOS process, the ideal characteristic impedance is found to be around 2 to 5Ω. Considering also the per square sheet resistance around 25mΩ, the achievable attenuation constant is found to be around 125m^{-1} to 300m^{-1}, almost an order of magnitude higher than that imposed by (12).

From this, it is clear that in order to work at an IC level, any salphasic clock distribution must implement loss compensation techniques. Given the maximum tolerated clock skew for the system, (12) and (13) may be used to determine the maximum acceptable attenuation constant of the lines used in the integrated clock distribution network.

By uniformly distributing negative conductance cells along the transmission line [28], [32], [35] the propagation constant γ for the line can be made as close as desired to be imaginary and, hence, the line will be loss compensated. The elementary cell for the lumped circuit model, assuming also the compensation technique, becomes similar with that of fig. 2. The R, L, C, G parameters are the per unit-length, intrinsic line parameters. The capacitance of the integrated clock transmission line is not given only by the physical characteristics of the line, but, in large proportion, by the clock loads. G_S represents the effect of the uniformly distributed negative conductance compensation cells and C_S is the parasitic capacitance associated with them. Both G_S and C_S are per unit-length parameters, given by the total number of active compensation cells that are used and the physical length of the line.

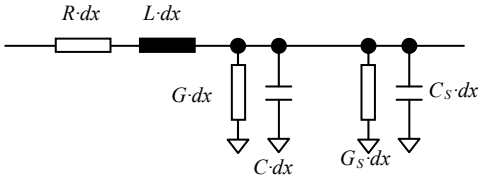

Figure 2. Elementary lumped-circuit model cell for the compensated line

Starting from the general expression of the propagation constant (14), the losses may be compensated if the real part of (14) is (very close to) zero:

$$\gamma = \sqrt{(R + j\cdot\omega\cdot L)\cdot(G + G_S + j\cdot\omega\cdot(C + C_S))} \tag{14}$$

By imposing for the negative conductance an expression like (15), the real part of the complex propagation constant becomes zero:

$$G_S = -\frac{R\cdot(C + C_S)}{L} - G \tag{15}$$

A critical aspect for the salphasic distribution is that all losses must be compensated independent of process or operating conditions. Any uncompensated shift in the operating point of the active circuit will result in the degradation of the salphasic standing wave configuration. Additionally, although the expression in (15) is independent of the operating frequency, in reality there are a variety of second order effects (like the skin effect, or the dielectric loss tangent) that can affect the needed compensation conductance. From this, the loss compensation circuit must be adjustable over an extended range, as proposed by the author in [36].

III. Bi-dimensional Slphasic Extensions

Although, it seems, the resonant or standing wave based distributions are capable of creating extended same-phase regions at a fraction of the power consumption of a standard solution, there is still room for improvements. A critical observation that can be made is that, as highlighted in [37], the clock distribution covers only a limited silicon area. The final driven clock tree leafs (where most of the total clock capacitance is situated) are using a classic buffered distribution, with the associated drawbacks.

As a salphasic distribution is not a self-oscillating network, the effective shape of the distribution is not critical to system operation. In fact, as first proposed in [26], the distribution can work also for generalized geometries. If integrated, such a configuration would be capable of distributing the zero-skew clock signal over the entire silicon area, completely eliminating the need for a standard distribution on the last levels. Introduced for the first time in [28] with limited theoretical background and then fully expended in [37-38] for the IC case, the bi-dimensional salphasic clock distribution can achieve the same final timing parameters as other resonant techniques but with lower power consumption and in an extended frequency range.

As seen in fig. 3, the model for the 2D configuration starts from the decomposition of the structure into an appropriate lumped-circuit model, depending on the excitation scheme. If the clock source is an equivalent extended generator that drives an entire edge of the structure, the model follows an orthogonal pattern [37]. For a point-like generator, the model follows a radial pattern [38]. For the general case, the orthogonal structure of fig. 3 may be used also for a point source excitation, however, the derivation of the theoretical model becomes difficult in that case.

An observation that can be made for all 2D lumped-circuit models – they may be regarded as many paralleled transmission lines, all driven by the same source.

Assuming an excitation along the Oy axis, the theoretical differential equations for the orthogonal structure, as derived in [37], show a close resemblance with those for simple transmission lines. This result was expected as there is no current circulation in a direction perpendicular to the wave travel direction, the propagating electromagnetic wave assuming a plane-wave pattern.

$$\frac{\partial^2}{\partial x^2}u(x,y) - \gamma^2\cdot u(x,y) = 0 \tag{16}$$

$$\frac{\partial^2}{\partial x^2}i(x,y) - \gamma^2\cdot i(x,y) = 0 \tag{17}$$

$$\gamma = \sqrt{(G_S + j\omega\cdot C_S)\cdot(R_S + j\omega\cdot L_S)} \tag{18}$$

The above equations represent the second order differential equations for the surface voltage (16) and surface current (17). The propagation constant is given by (18). For the considered model, since there is no variable current circulation along the Oy axis, the differential equations written with respect to the y variable can be discarded.

The parameters L_S, C_S, R_S and G_S from the propagation constant are the per unit-surface specific parameters. If the model uses the same quantization for both axes (i.e. Δx =

Δy), then the above parameters are identical with the per square parameters.

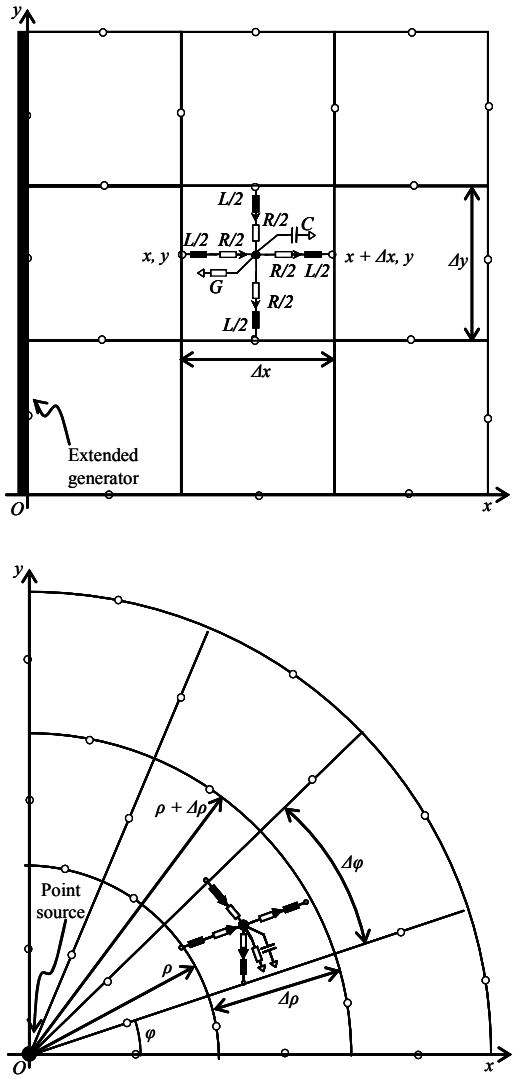

Figure 3. Surface decompositions into orthogonal and radial lumped-circuit models

Moving to the radial case, using a polar system of coordinates, the parameters for the lumped circuit of radial length *Δρ*, angular size *Δφ* and radial position *ρ* may be written as in [38]:

$$R = R_S \cdot \frac{1}{\rho} \cdot \frac{\Delta\rho}{\Delta\varphi} \tag{19}$$

$$L = L_S \cdot \frac{1}{\rho} \cdot \frac{\Delta\rho}{\Delta\varphi} \tag{20}$$

$$G = G_S \cdot \rho \cdot \Delta\rho \cdot \Delta\varphi \tag{21}$$

$$C = C_S \cdot \rho \cdot \Delta\rho \cdot \Delta\varphi \tag{22}$$

In the above (19) to (22) equations, L_S, C_S, R_S and G_S are the same, per square, surface parameters as used for the orthogonal case. As a note, the above relations where derived assuming infinitesimally small cells – i.e. with the radial length *Δρ* much smaller than the radial position *ρ*. Inspecting (19) and (20) it is clear that the system may not contain the origin, as both equations have a singularity for *ρ = 0*. However, assuming a generator with an infinitesimally small radius placed at the origin, starting from the lumped-circuit cell o fig. 4 it is possible to write for the surface voltage (23) and current (24) along the radial direction:

$$u\left(\rho + \frac{\Delta\rho}{2}, \varphi\right) = \frac{i(\rho,\varphi) - i(\rho + \Delta\rho, \varphi)}{G + j\omega \cdot C} \tag{23}$$

$$i(\rho,\varphi) = 2 \cdot \frac{u(\rho,\varphi) - u\left(\rho + \frac{\Delta\rho}{2}, \varphi\right)}{R + j\omega \cdot L} \tag{24}$$

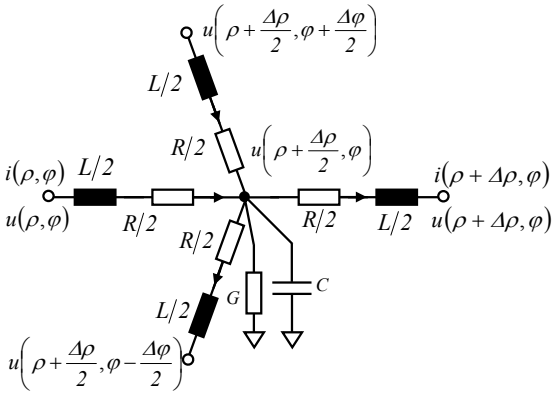

Figure 4. Elementary lumped-circuit model cell for the radial structure (with node voltages and branch currents)

Since the surface excitation is made by a point source, there is no current circulation along the angular coordinate and, hence, the equations written with respect to this coordinate may be discarded. Introducing the surface parameters as defined in (19) to (22) in (23) and (24) yields:

$$u\left(\rho + \frac{\Delta\rho}{2}, \varphi\right) = -\frac{i(\rho + \Delta\rho, \varphi) - i(\rho,\varphi)}{\Delta\rho \cdot \rho \cdot \Delta\varphi} \cdot \frac{1}{G_S + j\omega \cdot C_S} \tag{25}$$

$$i(\rho,\varphi) = -\frac{u\left(\rho + \frac{\Delta\rho}{2}, \varphi\right) - u(\rho,\varphi)}{\frac{\Delta\rho}{2}} \cdot \frac{\rho \cdot \Delta\varphi}{R_S + j\omega \cdot L_S} \tag{26}$$

In (25), if the considered cell has very small physical dimensions, the node voltage of the central point of coordinates *(ρ + Δρ / 2, φ)* may be approximated with the potential of the input node of coordinates *(ρ, φ)*. With this, both in (25) and (26) it is possible to recognize the first order derivatives of the surface's voltage and current. After further manipulation, the first order differential equations for the voltage (27) and current (28) may be written as:

$$\frac{\partial}{\partial\rho} u(\rho,\varphi) = -i(\rho,\varphi) \cdot \frac{R_S + j\omega \cdot L_S}{\rho \cdot \Delta\varphi} \tag{27}$$

$$\frac{\partial}{\partial\rho} i(\rho,\varphi) = -u(\rho,\varphi) \cdot \rho \cdot \Delta\varphi \cdot (G_S + j\omega \cdot C_S) \tag{28}$$

By taking the second derivative of (27) and (28), the resulting system of second order differential equations describes a cylindrical wave (again, as expected) [38].

$$\frac{\partial^2}{\partial\rho^2} u(\rho,\varphi) + \frac{1}{\rho} \cdot \frac{\partial}{\partial\rho} u(\rho,\varphi) - \gamma^2 \cdot u(\rho,\varphi) = 0 \tag{29}$$

$$\frac{\partial^2}{\partial\rho^2} i(\rho,\varphi) - \frac{1}{\rho} \cdot \frac{\partial}{\partial\rho} i(\rho,\varphi) - \gamma^2 \cdot i(\rho,\varphi) = 0 \tag{30}$$

It is interesting to note that the propagation constant *γ* has the same expression as (18) for the orthogonal case. This shows that, as stated before, the orthogonal model of fig. 3 may be used also for a point-source excitation.

For an ideal surface (i.e. with R_S and G_S both being zero or perfectly loss compensated, resulting in an imaginary propagation constant *γ* given by the phase constant *β*), the solution for the voltage wave is a linear combination of

Hankel functions of the first and second kinds and order 0 (i.e. linear combinations of Bessel functions with complex coefficients, again, of the first and second kinds). Since there is no closed-form definition for the functions, the solution for the voltage wave equation (29) may be written in integral form as in (31):

$$u(\rho) = -\frac{2 \cdot U_0^D}{j \cdot \pi} \int_0^{\infty} e^{j \cdot (\omega t - \beta \cdot \rho \cdot \cosh(\theta))} d\theta + \\ + \frac{2 \cdot U_0^R}{j \cdot \pi} \int_0^{\infty} e^{j \cdot (\omega t + \beta \cdot \rho \cdot \cosh(\theta))} d\theta \tag{31}$$

In (31), U_0^D and U_0^R stand for the direct and reverse complex voltages, as measured at the origin of the system. From an engineering point of view, an important aspect for a signal distribution using the modeled structure is the phase velocity of the propagating wave as this sets a relation between the needed salphasic termination impedance and the physical dimensions of the system. However, since there is no closed-form form for (31) it is not possible to write such a relation for the radial structure leaving as valid option only an approximation based on tabulated / computed values for the Bessel functions. At most, the solution given by (31) may be regarded as a family of waves (easily seen if the integrals are switched to Riemann infinite series representations), with each propagating wave dependent on the phase constant β and on the integration parameter θ. This result, however, is of no practical use as, for real systems, there is no physical possibility to separate the direct and the reflected waves found in (31). In fact, he radial system may be regarded as a collection of parallel connected transmission lines with an increasing line width resulting in a non-uniform characteristic impedance. From this, signal reflection takes place at every point of the system and not only at its periphery.

If the system is operated such as the direct and the reverse waves have equal amplitudes U_0 but there is a phase difference of $2 \cdot \varphi$ (for simpler relations) between them – the standing wave configuration may be described as in (32) by a combination of Bessel functions of the first and second kind and order 0:

$$u(\rho) = U_0 \cdot e^{-j \cdot \varphi} \cdot \cos(\varphi) \cdot \frac{4}{\pi} \int_0^{\infty} \sin(\beta \cdot \rho \cdot \cosh\theta) d\theta + \\ + U_0 \cdot e^{-j \cdot \varphi} \cdot \sin(\varphi) \cdot \frac{4}{\pi} \int_0^{\infty} \cos(\beta \cdot \rho \cdot \cosh\theta) d\theta \tag{32}$$

In the ideal salphasic case – that is $2 \cdot \varphi = 0$, the configuration of (32) reduces to the Bessel function of the first kind (i.e. the first term). If, however, this condition is not met, as the Bessel function of the second kind has a singularity in the origin, the second term in (32) may become the dominant one, at least for positions close to the generator. As the distributed signal's amplitude at the injection point may be, at most, equal with the open-circuit generator's amplitude, the presence of the second term in (32) translates in a steep dependence of the distributed signal's amplitude relative to the phase shift induced by the termination impedance. Furthermore, as the injected signal's amplitude depends on the ratio between the characteristic impedance of the structure and the generator's impedance, this further accentuates the steep conversion of load phase errors into amplitude variations. To compensate for this effect and to tolerate as much as possible the above phase errors, since the surface impedance may be quite low, the system would need a large signal driver with high impact on the power requirements.

With all the above considerations, the structure, as proposed in [26] proves to be un-attractive from a system's perspective.

As proposed in [38], the dependence of the characteristic impedance on the radial position may be compensated by artificially changing the surface parameters. The system will behave as if the wave propagation follows the simple case of plane-waves, similar with the orthogonal surface (and hence, the name proposed in [38] – pseudo-orthogonal structure).

Reference [38] showed that such a case allows easy distribution of the clock signal over the silicon area. Furthermore, the modified radial surface may be used in an inverted mode, with the generator moved to the periphery of the structure [38]. The advantage is there is only one termination impedance that must be matched to the resulting characteristic impedance. The extended generator can be formed easily with the aid of a small, classic distribution, or, as in [38], with another salphasic structure.

For the radial structure, the configuration proposed in [38] is not the single useful possibility. As new theoretical results are showing, by altering the surface's parameters in order to accentuate the dependence on the radial position as in (33) and (34), the proposed system will behave as if the propagation assumes a spherical wave pattern (as a note, by modifying the system's parameters, the radial structure becomes anisotropic and hence, it can support this pseudo-spherical pattern).

$$L_S'(\rho) = \frac{1}{\rho} \cdot L_{SS} \tag{33}$$

$$C_S'(\rho) = \rho \cdot C_{SS} \tag{34}$$

In (33) and (34) the parameters L_{SS} and C_{SS} represent the per square parameters of the initial surface adjusted for measurement unit conservation – e.g. the L_{SS} inductance is the per square inductance L_S multiplied with a standard length of 1m. With this, the variable pseudo-spherical unit-surface inductance $L'_S(\rho)$ has the correct unit (Henries) and shows an inverse dependence of the radial position ρ. Note that similar relations may be written for the loss inducing elements R'_S and G'_S.

Using (33) and (34) and repeating the steps used to determine the differential equations for the simple radial case, the first order differential equations for the voltage and current waves may be written as (35) and (36):

$$\frac{\partial}{\partial \rho} u(\rho, \varphi) = -i(\rho, \varphi) \cdot \frac{R_{SS} + j\omega \cdot L_{SS}}{\rho^2 \cdot \partial \varphi} \tag{35}$$

$$\frac{\partial}{\partial \rho} i(\rho, \varphi) = -u(\rho, \varphi) \cdot \rho^2 \cdot \partial \varphi \cdot (G_{SS} + j\omega \cdot C_{SS}) \tag{36}$$

By taking the second derivative and separating the surface voltage and current terms, relations (37) and (38) depict a spherical wave:

$$\frac{\partial^2}{\partial \rho^2} u(\rho, \varphi) + \frac{2}{\rho} \cdot \frac{\partial}{\partial \rho} u(\rho, \varphi) - \gamma^2 \cdot u(\rho, \varphi) = 0 \tag{37}$$

$$\frac{\partial^2}{\partial \rho^2} i(\rho, \phi) - \frac{2}{\rho} \cdot \frac{\partial}{\partial \rho} i(\rho, \phi) - \gamma^2 \cdot i(\rho, \phi) = 0 \tag{38}$$

The propagation constant γ from (37) and (38) is, in fact,

identical with that of the orthogonal case, given by (18). The advantage over the cylindrical wave is that the solution for the voltage wave has an closed-form form as in (39):

$$u(\rho,\varphi)=-\frac{U_0^D}{\gamma\cdot\rho}\cdot e^{-\gamma\cdot\rho}+\frac{U_0^R}{\gamma\cdot\rho}\cdot e^{\gamma\cdot\rho} \tag{39}$$

For a lossless or loss compensated structure (i.e. with the complex propagation constant γ imaginary, expressed as the phase constant β), assuming a total reflection at the far end (making thus the amplitude of the reflected wave $U_0{}^R$ equal with that of the direct wave $U_0{}^D$) such that at the generator's node the reflected wave is in phase with the direct one, the voltage standing wave configuration is given by (40):

$$u(\rho,\varphi)=\frac{U_0^D}{j\cdot\beta\cdot\rho}\cdot\left(-e^{-j\cdot\beta\cdot\rho}+e^{j\cdot\beta\cdot\rho}\right) \tag{40}$$

Using Euler's identity, the standing wave configuration becomes:

$$u(\rho,\varphi)=2\cdot U_0^D\cdot\operatorname{sinc}(\beta\cdot\rho) \tag{41}$$

It is evident in (41) that, again, the standing wave presents extended same-phase regions, given this time by the cardinal sine function. An advantage of the cardinal sine over the simple sine function is the double distance between the origin of the system and the first voltage node The useful area covered by the pseudo-spherical structure can be 4 times larger than for the pseudo-orthogonal one.

A further research topic regarding the pseudo-spherical structure is the influence of the incorrect phase shift introduced by the termination impedance. At first sight, the effect appears similar with that present at the un-modified system – i.e. a conversion of the phase error into standing wave amplitude variations, but without a detailed comparison between the structures, it is not possible to identify the better configuration with respect to this aspect. Anyway, since the wave equation solution has an closed-form form, in this regard, the proposed modified surface allows a simpler design procedure than the original structure.

For a practical system realization according to [38] or to the above pseudo-spherical structure it is not possible to directly follow the lumped circuit parameters variation laws (this would require the implementation of a continuous variation of the structure's parameters). Instead, a discrete approximation must be used.

For pseudo-orthogonal systems, a critical aspect of the discretization is that it has to assure a constant characteristic impedance, independent of the radial coordinate. A possible solution is to divide the surface along the radial direction ρ in several annuli of identical radial width (i.e. using a uniform radial step $\Delta\rho$) and along the angular coordinate φ with a fixed angular span $\Delta\varphi$. Each resulting annular sector may be regarded as a transmission line segment with the line parameters dependent on the sector's dimensions and position. Considering an annular sector as seen in fig. 3 for the radial excitation model, the segment inductance and capacitance may be calculated using (42) and (43):

$$L=\frac{L_S}{\Delta\varphi}\cdot\ln\left(1+\frac{\Delta\rho}{\rho}\right) \tag{42}$$

$$C=C_S\cdot\Delta\varphi\cdot\left(\rho\cdot\Delta\rho+\frac{\Delta\rho^2}{2}\right) \tag{43}$$

In (42) and (43) L_S and C_S represent the per square inductance and capacitance parameters. As a note, the loss inducing components R and G have a similar behavior with that of (42) and (43). Given the inverse dependence of the radial coordinate in (42), the model cannot contain the origin of the system but can be made arbitrarily close to it by choosing a small enough radial step $\Delta\rho$. With this, the first annular sector starts at the radial coordinate ρ_0 and its parameters will be considered as reference parameters for the rest of the annular sectors. By taking the ratio between the values for an arbitrary radial coordinate ρ and for the reference segment, the discrete scaling of the per square surface results as:

$$L_S^{'}=L_S\cdot\ln\left(1+\frac{\Delta\rho}{\rho_0}\right)\Big/\ln\left(1+\frac{\Delta\rho}{\rho}\right) \tag{44}$$

$$C_S^{'}=C_S\cdot\frac{2\cdot\rho_0+\Delta\rho}{2\cdot\rho+\Delta\rho} \tag{45}$$

Parameters $L^{'}_S$ and $C^{'}_S$ from (44) and (45) represent the per square parameters for the pseudo-orthogonal surface as defined in [38]. If the radial width $\Delta\rho$ goes to zero, the variation laws given by (44) and (45) reduce to those defined in [38] for the theoretical model.

From a physical point of view, the adjustment of the lumped circuit model parameters as given by (44) and (45) (or given by a similar model for the pseudo-spherical case) may be achieved by changing the shape of the clock distribution along the radial distance, as seen in fig.5.

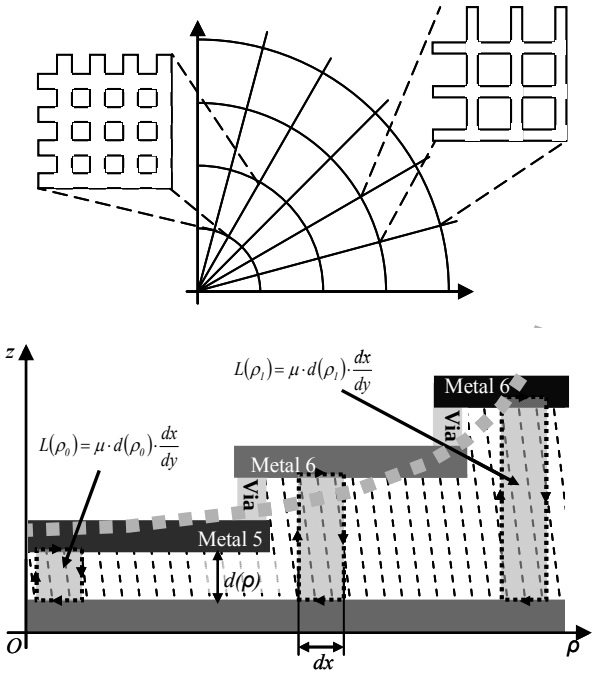

Figure 5. Adjustment of the per unit-area resistance and inductance by using different mesh structure and several metal layers

For instance, the adjustment of the per unit-area resistance may be realized by having a metal mesh with different eye openings and densities, according to the position coordinate.

For the adjustment of the per unit-area inductance, one can start from the observation that the inductance depends on the magnetic loop area – in order to increase the area, the distance between the conductive levels must also increase. By using several metal layers, as depicted in fig. 5, the elementary inductance can be shaped to follow the desired law. The adjustment of the capacitance can be easily

achieved by the use of dummy clock loads, distributed unevenly across the IC's surface and, thus, poses no specific problem.

IV. Simulation Results

Similar with [37-38], the structures simulated using HSpice showed the formation of the expected standing waves with a voltage anti-node at the generator's side. Although not ideal for a normal clock distribution, the results of fig. 6 are presented for an excitation frequency where the pattern has a voltage node placed in the middle of the surface – i.e. the length of the structure corresponds to half of the wavelength. This configuration was chosen only for graphic purposes. For an integrated circuit case, the best configuration is to use a structure with a length less than a quarter of the wavelength. In this way all of the clock driven points see a sufficient signal amplitude.

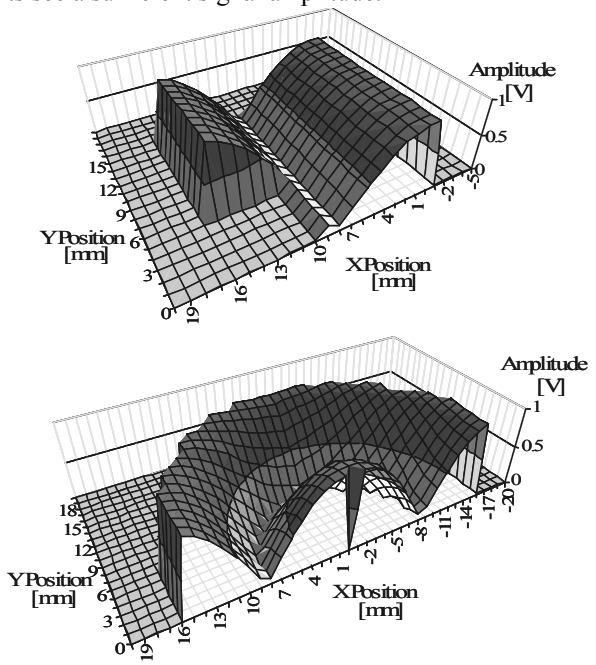

Figure 6. Salphasic standing wave configuration for orthogonal and (pseudo-orthogonal) radial structures

As a note, the radial structure was used in an inverted mode – i.e. the surface is driven as in [38] by an extended generator placed at the periphery of the system. Additionally – it is important to stress that a designer targeting a radial salphasic structure must strive to create a surface as symmetric as possible in order to a void excitation modes along the angular direction. The same is true also for orthogonal structures where excitation modes along a direction parallel with the extended generator must be avoided.

For the orthogonal case, the simulated structure has a width of 15mm (on the generator's extended node) and a length of 15mm for the long edge and 10mm for the short edge. The width of the short edge is 5mm. The radial structure has a diameter of 16mm with the observation that the first millimeter around the origin was not simulated (to avoid the singularity in the surface's parameters). This makes the effective radial length of the surface to be 15mm.

Both simulated structures are using a decomposition into square elementary cells. Each cell has a size of 1/3mm by 1/3mm. Given the shapes of the simulated structures, a total of 1800 cells were used for the orthogonal model and about 3600 cells for the radial structure. For ease of simulation, the electrical model for the cell follows that of fig. 7, being a lossless structure.

The radial case uses the modified parameters structure, emulating a pseudo-orthogonal system. To this end, the surface was subdivided in 15 annuli as seen in fig. 8 with each annulus having a different set of per square parameters, according to (44) and (45). Correlating with the sizes of the unit cells, this division translates in 3 unit cells per annulus along a radial direction. Fig. 8 also shows the effect of the surface discretization according to an orthogonal model, resulting in a rugged contour for the considered annuli. Starting from the first annulus (considered as the reference segment), the parameters of consecutive segments are scaled by approximately 1.71, 2.41, 3.10, 3.80, 4.5, 5.19, 5.88, 6.58, 7.27, 7.97, 8.66, 9.35, 10.05 and 10.74 for the inductance and by 0.6, 0.428, 0.333, 0.273, 0.231, 0.2, 0.177, 0.158, 0.143, 0.13, 0.12, 0.111, 0.103 and 0.097 for the capacitance.

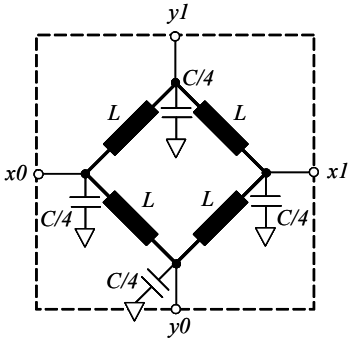

Figure 7. Unit surface cell for Spice simulation

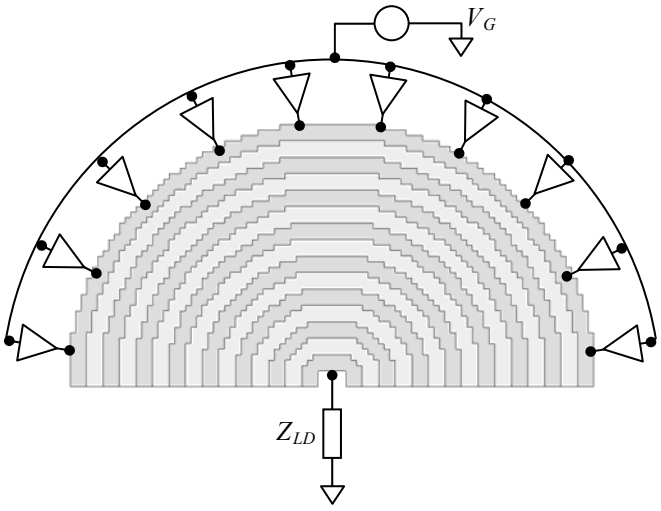

Figure 8. Simulated radial salphasic structure with a decomposition into consecutive – different parameters – annuli

Since the radius of the structure corresponds to half of the wavelength, the termination impedance Z_{LD} should be infinite (i.e. left open) in order to place the voltage anti-node at the generator. This holds also for the orthogonal structure on the longer edge. For the shorter edge, a distributed capacitive load is necessary in order to compensate the electrical length difference. Since the behavior of the orthogonal surface is similar with that of a simple transmission line, the value of the needed capacitance may be calculated using the same mathematical formalism.

The electrical parameters for the elementary cell are L = 6.37pH total inductance and C = 1.8pF total capacitance, yielding a characteristic impedance for the cell of 1.88Ω. Since the width of the orthogonal structure is 15mm, the characteristic impedance of the entire orthogonal system is 41.7mΩ, that is, the paralleled characteristic impedance of 45 transmission lines, each of 1.88Ω.

For the radial case, the impedance may be calculated based on the number of elementary cells that can be fitted into the length of the chord situated at the average radius of the first annulus. For the simulated structure, this number is 14, resulting in a characteristic impedance around 134mΩ. Both circuit configurations were driven from an extended clock buffer (unit buffers uniformly distributed along the generator's edge) with an equivalent output impedance of about 0.5Ω for the orthogonal case, as in [37] and with an output impedance of 1Ω for the radial case, similar with [38].

The results of both fig. 6 and fig. 8 are obtained at a clock frequency of 3.28GHz.

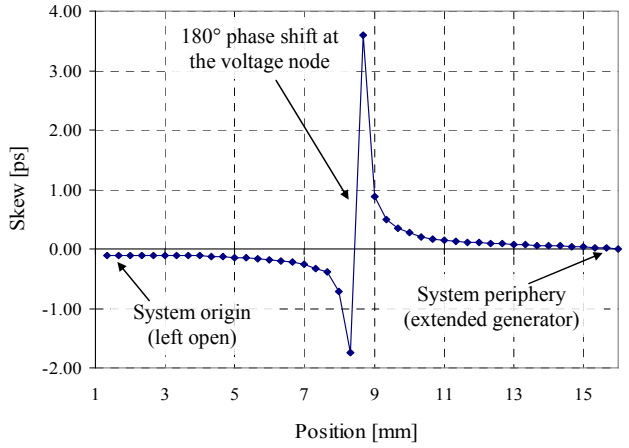

Figure 9. Skew along a radial direction of the pseudo-orthogonal structure

Inspecting fig. 8, depicting the simulated signal skew along a radial direction for the pseudo-orthogonal structure, it can be seen that the maximum signal skew realized by the simulated structure is around 3.6ps (i.e. 1.18% of the signal's period), with steep slopes around the voltage node's position. From a real system's perspective, as practical IC applications are not expected to use regions around the voltage nodes, these steep slopes translate in much lower achievable skews – for instance, for systems having a radius of only 4mm, the maximum skew error is expected to be at least one order of magnitude lower – i.e. in the sub-picoseconds range (from fig.8, for points having a radial coordinate of 12mm – the expected skew is found to be around 0.1ps).

Reference [37] made also a comparison between the power requirements at 3.28GHz and 1V VDD for the simulated structure (1.1W), compared with a buffered clock distribution (55W), showing a net advantage towards the salphasic clock distribution.

V. Conclusions

A major difference between the salphasic clock distribution and other standing wave based configurations is the ability to generate the in-phase clock signal over the entire silicon area, without using standard distribution techniques for the highly loaded nodes. At most, the standard technique is used to generate the extended generators that are driving the salphasic network – a critical observation that must be made is that, by design, the input of the salphasic structure presents a no-load condition for the signal generator. This means that, although the input clock source sees the entire silicon area, it can be designed to be much smaller than for any other clock distribution.

By generating a standing wave pattern over the entire silicon area, a bi-dimensional salphasic structure shows a net improvement for the power consumption as the whole clock load capacitance is an integral part of the clock distribution network.

As a new theoretical result for radial structures, the present paper showed that by accentuating the dependence of the R, L, C, G parameters of the lumped circuit model on the radial position, the system assumes a pseudo-spherical wave propagation mode. This allows the formation of a standing wave according to a cardinal sine function, with the main advantage of a double length between the origin and the first voltage node.

The integration of the salphasic structure on the silicon die is not a straightforward process since the transmission lines structures that can be built on the silicon substrate usually have high losses. However, starting from already existing techniques and structures and modifying them according to the salphasic distribution's requirements (i.e. the need to adjust the negative conductance over an extended range to compensate for the operating point drifts [36]), it was shown in [28] that the salphasic concept can be not only implemented in ICs, but also made highly efficient [37-38] and here, even compared to other, state of the art, standing wave based techniques.

Furthermore, regarding this topic, the present paper set for the first time a design constraint for the attenuation constant which still maintains the phase error in the standing wave pattern below the imposed clock skew limits.

As a last observation, for the radial structures with a simulated behavior (pseudo-orthogonal or pseudo-spherical), the present paper also provided theoretical support and practical methods on how to adjust the needed surface parameters.

References

[1] E. G. Friedman, "Clock distribution networks in synchronous digital integrated circuits," Proceedings of the IEEE, vol. 89, no. 5, pp. 665–692, May 2001. doi:10.1109/5.929649.

[2] E. De Man, M. Schöbinger, "Power Dissipation in the Clock System of highly pipelined ULSI CMOS Circuits", Proceedings of the International Workshop on Low-Power Design, Apr. 1994.

[3] H. Kojima, S. Tanaka, K. Sasaki,*"Half-Swing Clocking Scheme for 75% Power Saving in Clocking Circuitry"*, Symposium on VLSI Circuits, Digest of Technical Papers, pp. 432-435, 1994. doi:10.1109/VLSIC.1994.586193.

[4] H. Kawaguchi, T. Sakurai, "A reduced clock-swing flip-flop (RCSFF) for 63% power reduction," IEEE Journal of Solid-State Circuits, vol. 33, no. 5, pp. 807–811, May 1998. doi:10.1109/4.668997.

[5] K. D. Boese, A. B. Kahng, "Zero-Skew Clock Routing Trees With Minimum Wirelength", Proceedings of the 5th Annual IEEE International ASIC Conference and Exhibit, pp. 17-21, Sep. 1992. doi:10.1109/ASIC.1992.270316.

[6] G. M. Blair, "Skew-Free Clock Distribution for Standard-Cell VLSI Designs", Proceedings of IEE Circuits, Devices and Systems, vol. 139, no 2, pp 265-268, Apr. 1992.

[7] Y. P. Chen, D. F. Wong, "An Algorithm for Zero-Skew Clock Tree Routing with Buffer Insertion", Proceedings of European Design and Test Conference 1996 ED&TC 96, pp. 230-236, 11 – 14 March, 1996. doi:10.1109/EDTC.1996.494154.

[8] T. Fischer, J. Desai, B. Doyle, S. Naffziger, B. Patella, "A 90-nm Variable Frequency Clock System for a Power-Managed Itanium Architecture Processor," IEEE Journal of Solid-State Circuits, vol. 41, no. 1, pp. 218–228, Jan. 2006. doi:10.1109/JSSC.2005.859879.

[9] V. Gutnik, A. P. Chandrakasan, "Active GHz clock network using distributed PLLs," IEEE Journal of Solid-State Circuits, vol. 35, no. 11, pp. 1553–1560, Nov. 2000. doi:10.1109/4.881199.

[10] H.-A. Tanaka, A. Hasegawa, H. Mizuno, T. Endo, "Synchronizability of distributed clock oscillators," IEEE Transactions on Circuits and Systems I: Fundamental Theory and Applications, vol. 49, no. 9, pp. 1271–1278, Sep. 2002. doi:10.1109/TCSI.2002.802361.

[11] A. Carpenter, "Design and Use of High-Speed Transmission Line Links for Global On-Chip Communication", PhD Dissertation, University of Rochester, 2012.

[12] S. Naffziger, B. Stackhouse, T. Grutkowski, D. Josephson, J. Desai, E. Alon, M. Horowitz, "The Implementation of a 2-Core, Multi-Threaded Itanium Family Processor," IEEE Journal of Solid-State Circuits, vol. 41, no. 1, pp. 197–209, Jan. 2006. doi:10.1109/JSSC.2005.859894.

[13] E. Takahashi, Y. Kasai, M. Murakawa, T. Higuchi, "Post-Fabrication Clock-Timing Adjustment Using Genetic Algorithms," IEEE Journal of Solid-State Circuits, vol. 39, no. 4, pp. 643–650, Apr. 2004. doi:10.1109/JSSC.2004.824706.

[14] R.J. Riedlinger, R. Bhatia, L. Biro, B. Bowhill, E. Fetzer, P. Gronowski, T. Grutkowski, "A 32nm 3.1 billion transistor 12-wide-issue Itanium® processor for mission-critical servers", Digest of Technical Papers, 2011 IEEE International Solid-State Circuits Conference (ISSCC), pp. 84-86, 20-24 February 2011. doi:10.1109/ISSCC.2011.5746230.

[15] P. Sedcole, J.S. Wong, P.Y.K. Cheung, "Modelling and compensating for clock skew variability in FPGAs", International Conference on ICECE Technology, 2008, pp. 217-224, 8-10 Dec. 2008. doi:10.1109/FPT.2008.4762386.

[16] T. Susa, M. Murakawa, E. Takahashi, T. Furuya, T. Higuchi, "Post-Fabrication Clock-Timing Adjustment for Digital LSIs Ensuring Operational Timing Margins", 8th International Conference on Hybrid Intelligent Systems, 2008, pp. 907-910, 10-12 Sep. 2008. doi:10.1109/HIS.2008.139.

[17] YS. Kwon, IC. Park, CM. Kyung, "A New Single-Clock Flip-Flop for Half-Swing Clocking", Proceedings of the ASP-DAC '99 Design Automation Conference, Asia and South Pacific, vol. 1, pp. 117 - 120, 18-21 Jan. 1999. doi:10.1109/ASPDAC.1999.759727.

[18] C. Kim, S.-M. Kang, "A low-swing clock double-edge triggered flip-flop," IEEE Journal of Solid-State Circuits, vol. 37, no. 5, pp. 648–652, May 2002. doi:10.1109/4.997859.

[19] D. Levacq, M. Yazid, H. Kawaguchi, M. Takamiya, T. Sakurai, "Half VDD Clock-Swing Flip-Flop with Reduced Contention for up to 60% Power Saving in Clock Distribution", 33rd European Solid State Circuits Conference ESSCIRC 2007, pp. 190 - 193, 11-13 Sep. 2007. doi:10.1109/ESSCIRC.2007.4430277.

[20] K. Mohammad, B. Liu, S. Agaian, "Energy efficient swing signal generation circuits for clock distribution networks", IEEE International Conference on Systems, Man and Cybernetics SMC 2009, pp. 3495 – 3498, 11-14 Oct. 2009. doi:10.1109/ICSMC.2009.5346775.

[21] S. E. Esmaeili, A. J. Al-Kahlili,, G. E. R. Cowan, "Low-Swing Differential Conditional Capturing Flip-Flop for LC Resonant Clock Distribution Networks," IEEE Transactions on Very Large Scale Integration (VLSI) Systems, vol. 20, no. 8, pp. 1547–1551, Aug. 2012. doi:10.1109/TVLSI.2011.2158613.

[22] A. J. Drake, K. J. Nowka, T. Y. Nguyen, J. L. Burns, R. B. Brown, "Resonant clocking using distributed parasitic capacitance," IEEE Journal of Solid-State Circuits, vol. 39, no. 9, pp. 1520–1528, Sep. 2004. doi:10.1109/JSSC.2004.831435.

[23] S. C. Chan, K. L. Shepard, P. J. Restle, "Uniform-phase uniform-amplitude resonant-load global clock distributions," IEEE Journal of Solid-State Circuits, vol. 40, no. 1, pp. 102–109, Jan. 2005. doi:10.1109/JSSC.2004.838005.

[24] F. O'Mahony, C. P. Yue, M. A. Horowitz, S. S. Wong, "A 10-GHz global clock distribution using coupled standing-wave oscillators," IEEE Journal of Solid-State Circuits, vol. 38, no. 11, pp. 1813–1820, Nov. 2003. doi:10.1109/JSSC.2003.818299.

[25] M. Shiozaki, M. Sasaki, A. Mori, A. Iwata, H. Ikeda, "20GHz uniform-phase uniform-amplitude standing-wave clock distribution," IEICE Electronics Express, vol. 3, no. 2, pp. 11–16, 2006. doi:10.1587/elex.3.11.

[26] V. L. Chi, "Salphasic distribution of clock signals for synchronous systems," IEEE Transactions on Computers, vol. 43, no. 5, pp. 597–602, May 1994. doi:10.1109/12.280806.

[27] V. L. Chi, "Salphasic Distribution of Timing Signals for the Synchronization of Phisically Separated Entities", US patent US5387885, 7 Feb., 1995.

[28] A. Paşca, "Probleme specifice ce apar în reţelele de distribuţie de clock (Specific problems in clock distribution networks)", MSc dissertation, "Politehnica" University, Timişoara, Romania, 2006.

[29] K. Moez, M. Elmasry, "A New Loss Compensation Technique for CMOS Distributed Amplifiers," IEEE Transactions on Circuits and Systems II: Express Briefs, vol. 56, no. 3, pp. 185–189, Mar. 2009. doi:10.1109/TCSII.2009.2015362.

[30] M. Yazgi, A. Toker, B. S. Virdee, "A new negative resistance circuit and an application for loss compensation in a distributed amplifier," Journal of Analog Integrated Circuits and Signal Processing, vol. 60, no. 3, pp. 215–220, Sep. 2009. doi:10.1007/s10470-009-9279-9.

[31] A. Ghadiri, "Design of Active-Based Passive Components for Radio Frequency Applications", PhD Dissertation, University of Alberta, 2011.

[32] M. Bussmann, U. Langmann, "Active compensation of interconnection losses for multi-GHz clock distribution networks," IEEE Transactions on Circuits and Systems II: Analog and Digital Signal Processing, vol. 39, no. 11, pp. 790–798, Nov. 1992. doi:10.1109/82.204127.

[33] B. Ravelo, A. Perennec, M. Le Roy, "Application of Negative Group Delay Active Circuits to Reduce the 50% Propagation Delay of RC-Line Model", 12th IEEE Workshop on Signal Propagation on Interconnects, 2008, pp. 1-4, May 2008. doi:10.1109/SPI.2008.4558347.

[34] B. Ravelo, A. Perennec, M. Le Roy, "Equalization of Interconnect Propagation Delay with Negative Group Delay Active Circuits", 11th IEEE Workshop on Signal Propagation on Interconnects (SPI'07), May 2007, pp.15-18, 2007. doi:10.1109/SPI.2007.4512196.

[35] A. P. Jose, K. L. Shepard, "Distributed Loss-Compensation Techniques for Energy-Efficient Low-Latency On-Chip Communication," IEEE Journal of Solid-State Circuits, vol. 42, no. 6, pp. 1415–1424, Jun. 2007. doi:10.1109/JSSC.2007.897165.

[36] A. Paşca, "Negative Impedance Converter Circuits for Integrated Clock Transmission Lines Loss Compensation", Buletinul ştiinţific al Universităţii "Politehnica" din Timişoara, seria Electronică şi Telecomunicaţii, Tom 54(68), Fascicola 1, 2009.

[37] A. Paşca, "Clock Distribution Using a Bi-dimensional Orthogonal Salphasic Structure", Proceedings of the International Conference on Circuits, Systems, Signal Processing, Communications and Computers (CSSCC 2015), pp. 40-47, Viena, 15-17 March 2015.

[38] A. Paşca, "Bi-dimensional Radially-Salphasic (Standing Wave) Clock Distribution", 2014 IEEE 20th International Symposium for Design and Technology in Electronic Packaging (SIITME), pp. 157-162, 23-26 October, 2014. doi:10.1109/SIITME.2014.6967017.